Journal of Applied Physics

RESEARCH ARTICLE | MARCH 28 2024

Selective modulation of electronic transport in VO_2 induced by 10 keV helium ion irradiation

Special Collection: Phase-change Materials and Their Applications

Rebeca M. Gurrola ; John M. Cain ; Sangheon Oh ; Timothy D. Brown ; Fatme Jardali ; Ryan M. Schoell ; Digvijay R. Yadav ; Jiaqi Dong; Christopher M. Smyth ; Matt Pharr ; Suhas Kumar ; Kelvin Xie; Khalid Hattar ; A. Alec Talin ; Tzu-Ming Lu ; Patrick J. Shamberger

Check for updates

J. Appl. Phys. 135, 125109 (2024)
https://doi.org/10.1063/5.0189562

View Online
Export Citation

Articles You May Be Interested In

Manipulating the metal–insulator transitions and thermoelectric bi-functionality for correlated vanadium dioxide pellets

Appl. Phys. Lett. (July 2024)

Revealing the role of high-valence elementary substitution in the hydrogen-induced Mottronic transitions of vanadium dioxide

Appl. Phys. Lett. (February 2024)

03 March 2025 14:48:33

Nanotechnology & Materials Science
Optics & Photonics
Impedance Analysis
Scanning Probe Microscopy
Sensors
Failure Analysis & Semiconductors

Unlock the Full Spectrum.
From DC to 8.5 GHz.
Your Application. Measured.
Find out more
Zurich Instruments

AIP Publishing

Journal of Applied Physics ARTICLE pubs.aip.org/aip/jap

Selective modulation of electronic transport in VO_2 induced by 10 keV helium ion irradiation

Cite as: J. Appl. Phys. **135**, 125109 (2024); doi: 10.1063/5.0189562
Submitted: 29 November 2023 · Accepted: 5 March 2024 ·
Published Online: 28 March 2024

View Online Export Citation CrossMark

Rebeca M. Gurrola,[1] John M. Cain,[2] Sangheon Oh,[3] Timothy D. Brown,[3] Fatme Jardali,[1] Ryan M. Schoell,[4] Digvijay R. Yadav,[1] Jiaqi Dong,[1] Christopher M. Smyth,[2] Matt Pharr,[5] Suhas Kumar,[3] Kelvin Xie,[1] Khalid Hattar,[4,6] A. Alec Talin,[3] Tzu-Ming Lu,[4] and Patrick J. Shamberger[1,a)]

AFFILIATIONS

[1]Department of Materials Science and Engineering, Texas A&M University, College Station, Texas 77843, USA
[2]Sandia National Laboratories, Albuquerque, New Mexico 87185, USA
[3]Sandia National Laboratories, Livermore, California 94550, USA
[4]Center for Integrated Nanotechnologies, Sandia National Laboratories, Albuquerque, New Mexico 87123, USA
[5]Department of Mechanical Engineering, Texas A&M University, College Station, Texas 77843, USA
[6]Department of Nuclear Engineering, University of Tennessee, Knoxville, Tennessee 37996, USA

Note: This paper is part of the special topic, Phase-change Materials and Their Applications.
[a)]**Author to whom correspondence should be addressed:** patrick.shamberger@tamu.edu

03 March 2025 14:48:33

ABSTRACT

Vanadium dioxide (VO_2) manifests an abrupt metal–insulator transition (MIT) from monoclinic to rutile phases, with potential use for tunable electronic and optical properties and spiking neuromorphic devices. Understanding pathways to modulate electronic transport in VO_2, as well as its response to irradiation (e.g., for space applications), is critical to better enable these applications. In this work, we investigate the selective modulation of electronic transport in VO_2 films subject to different 10 keV helium ion (He^+) fluences. Under these conditions, the resistivity in the individual monoclinic and rutile phases varied by 50%–200%, while the MIT transformation temperature remains constant within 4 °C independent of irradiation fluence. Importantly, different trends in the resistivity of the monoclinic and rutile phases were observed both as a function of total He fluence as well as in films grown on different substrates (amorphous SiO_2/Si vs single crystal Al_2O_3). Through a combination of measurements including majority carrier sign via Seebeck, low frequency noise, and TEM, our investigation supports the presence of different kinds of point defects (V in; O in), which may arise due to grain boundary defect interactions. Our work suggests the utility of He irradiation for the selective modulation of VO_2 transport properties for neuromorphic, in contrast to other established but non-selective methods, like doping.

© 2024 Author(s). All article content, except where otherwise noted, is licensed under a Creative Commons Attribution-NonCommercial 4.0 International (CC BY-NC) license (https://creativecommons.org/licenses/by-nc/4.0/). https://doi.org/10.1063/5.0189562

I. INTRODUCTION

Vanadium dioxide (VO_2), a strongly correlated electron system, exhibits a metal–insulator transition (MIT) at a critical temperature (T_{cr}) of 340 K, resulting in 1–4 orders of magnitude in resistance switching.[1,2] The non-linear electrical transport behavior near the MIT is advantageous for neuromorphic applications as a means to mimic the spiking behavior of neurons,[3] as demonstrated recently in simple neuronal circuits, which exhibit a broad array of oscillatory and spiking characteristics.[4] Despite the knowledge of how several aspects of the MIT can be modified, independent control over the charge transport and on–off ratios in both phases has not been realized. Implementation of VO_2 into neuromorphic applications requires an understanding of the electrical behavior.

While the change in charge transport between insulating and metallic phases is dominated by a transition from localized to delocalized electrons tied to the dimerization of the V^{4+} ions, charge transport in a VO_2 film can be further modified by the degree of crystallinity[5] or the presence of extrinsic or intrinsic defects.[6,7] These features can significantly affect the resistivity of either the high-symmetry rutile metallic phase (ρ_R)[8] or the low-symmetry monoclinic insulating phase (ρ_{M1}),[5] resulting in a decrease in the resistivity of both phases up to 2 orders of magnitude. Upon

irradiation, or the presence of extrinsic defects, near complete quenching of the transition can occur.[9] This leads to a wide range of on-to-off ratios, reaching up to 1×10^4 in ordered VO_2 films. Despite the knowledge of how several aspects of the MIT can be modified, independent control over the charge transport and on–off ratios in both phases is difficult to realize. Just as a detailed understanding of electronic transport in traditional semiconductors is critical for the design of integrated circuits, the implementation of VO_2 into neuromorphic applications also requires a detailed understanding of the electrical behavior as well as approaches to modify it.

Electronic transport in VO_2 thin films varies greatly because of the interplay between structural properties including orientation, residual strain, grain size, and inherent defects such as grain boundaries. In particular, with VO_2 deposition on TiO_2 substrates, changes in resistivity are due to nano-scale cracks as a form of strain relaxation,[10] formation of a $(V,Ti)O_2$ solid solution at the substrate film interface,[11] and changes in orbital occupancy.[12]

Growth of epitaxial VO_2 on Al_2O_3 (0001) with varying Ar to O_2 gas flow ratios during film growth greatly decreased the ρ_{M1} for films, this was attributed to the accumulation of V interstitials and an increase in the carrier density.[13] A study on the growth of polycrystalline VO_2 on Si_3N_4/Si at different thicknesses attributed the shifts in ρ_{M1} and ρ_R to a difference in the grain size. With smaller grains, the increase in grain boundaries was proposed to result in additional levels in the bandgap and a lowering of the resistivity of the low-symmetry M1 phase. The decrease in ρ_R was assumed to be due to the increase in grain boundary scattering.[8]

Further development of neuromorphic devices based on the MIT in VO_2 requires precise control over the resistivity ratio between the insulating (low-symmetry M1) and the metallic (high-symmetry R) phases of VO_2 as well as independent control over charge transport in these phases. The use of lattice strain, as described above, is not a selective method to tune the transformation as multiple aspects of the MIT are also changed. A notable exception to this trend is single crystal VO_2 growth on Si_3N_4/Si[8] and single crystal VO_2 grown on TiO_2 (001) and Al_2O_3 (0001).[14] The latter paper uses postdeposition treatment and varies the film thickness; however, these results are very different from similar studies[10,13] that focused on changing film thickness.

Ion implantation, the spatially controlled introduction of chemical dopants and structural defects through the acceleration of charged particles into a film, is a common strategy to modulate charge carrier concentrations in semiconductors.[15,16] Similarly, the ion irradiation of VO_2 with various charged or uncharged particles without subsequent annealing generates different types and concentrations of lattice defects, which could alter the MIT, and/or the charge transport in either high- or low-symmetry phases. Previous studies have investigated ion implantation and irradiation in VO_2, although these studies have primarily been motivated from the perspective of modulating the characteristics of the MIT (Fig. 1).

Exposure of VO_2 films to energetic particles tends to introduce defect populations, altering material properties and modulating the transformation behavior of the film (Table I). While a variety of different ions and energies have been used to modify the MIT, none of the methods were selective and modified the T_{MIT}, ρ_{M1}, ρ_R, and overall transition sharpness in some cases to the point of amorphization. Furthermore, previous studies have also not compared the irradiation of films with different microstructures. Whereas previous studies have focused on exploiting one design variable, we propose interrogating the interactions among lattice strain, the degree of crystallinity, and engineered defect populations.

The present study reports the effect of low-energy He^+ irradiation at different ion beam fluences on the electrical transport properties of thin VO_2 films in low- and high-symmetry phases. The low-energy He^+ irradiation introduces different defect populations into the film in an areal uniform distribution, without chemically altering its composition due to the immiscibility of the He in the VO_2 films. We investigate the impact of irradiation on the electrical transport in both polycrystalline VO_2 films grown on an amorphous SiO_2 layer as well as quasi-epitaxial films grown on a lattice-matched Al_2O_3 (0001) substrate. Herein, we demonstrate that the resistivity of the metallic phase in polycrystalline VO_2 films increases by approximately 200% relative to the initial film resistivity. In contrast, the resistivity of the metallic phase in quasi-epitaxial VO_2 films remains nearly unchanged, while the resistivity of the insulating phase decreases by nearly 50% relative to the initial film resistivity. These trends are explained by the nature of defects created in both films and the different grain boundary–defect

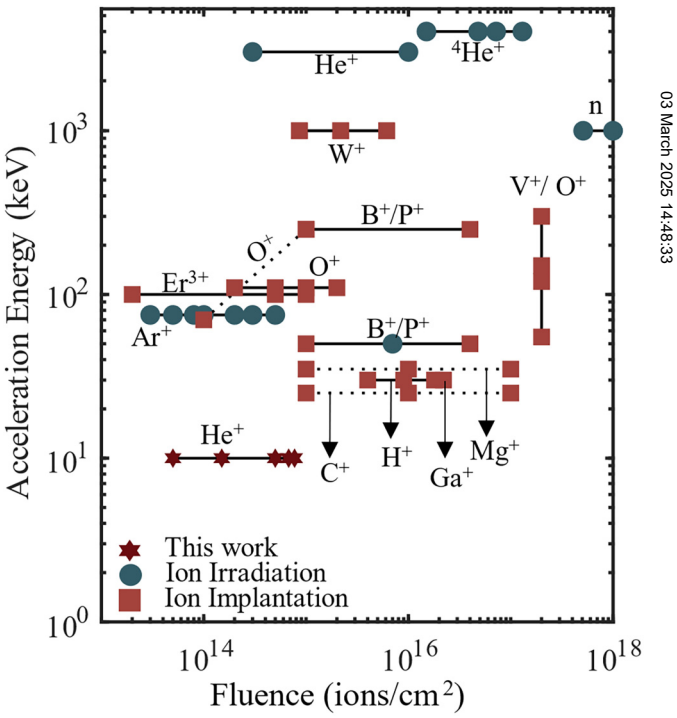

FIG. 1. Schematic describing literature values for the irradiation of VO_2 either for ion implantation (C^+,[17] O^+,[18–20] Cs^+,[21] B^+,[22] P^+,[22] W^+,[23,24] Mg^+,[17,25] Er^{3+},[26] Au^+,[27] Ga^+[28]) or for ion irradiation (with largely non-reactive particles, including $^4He^+$[17]/He^+,[29] H^+,[30] Ar^+,[21,31]). Lines connect the data points from a single study at a common acceleration voltage. The ion species utilized in this study is included in the plot.

03 March 2025 14:48:33

© Author(s) 2024

TABLE I. Summary of previous results of irradiation on electrical transport in VO_2.

Substrate	Ions	Energy (keV)	ρ_{M1}	ρ_R	T_{cr}	Defects observed	Reference
CaF_2, Al_2O_3	H^+	30	decrease	No effect	Decrease	V,O displacements	30
Al_2O_3	Ar^+	75	n.d.	n.d.	Decrease	Point defects,	21
	Cs^+	190				Frenkel pairs amorphization	
n/a (nanowires)	He^+	30	decrease	Increase	Decrease	Point defects	63
Al_2O_3	O^+	110	decrease	Decrease	Decrease	Point defects, defect clusters	18

n.d.—Not determined

interactions. The present study enables an understanding of the behavior of devices based on VO_2 when exposed to energetic ionized particles, thereby introducing various types of defects and altering the majority charge carrier concentration and mobility. It opens the possibility of designing novel non-linear transport behavior or further amplifying the resistivity differences between the on and off states of VO_2 devices.

II. EXPERIMENTAL

A. Thin film deposition

VO_2 films with a thickness of 100 nm were grown on single crystal Al_2O_3 (0001) substrates and on silicon substrates capped with 100 nm thick thermal oxide (SiO_2/Si). Films were grown by DC magnetron sputtering from a metallic vanadium target (99.95% pure) at 200 W, in a reactive Ar/O_2 atmosphere. Prior to deposition, substrates were sonicated in acetone for 30 min, followed by rinsing with methanol and isopropyl alcohol. Subsequently, the substrates were dried using compressed air. Deposition occurred at a substrate temperature of 600 °C, and a pressure of 2 mTorr, with Ar and O_2 flow rates of 20 and 4.6 ml min^{-1}, respectively. Postdeposition, the films were annealed for 1.5 h under vacuum at 600 °C to improve crystallinity.

B. Structural characterization

The structure and morphology of the films were subsequently analyzed using x-ray diffraction (XRD), atomic force microscopy (AFM), Raman spectroscopy, and transmission electron microscopy (TEM). Out of plane XRD scans were obtained using a Rigaku diffractometer with parallel beam geometry. Diffraction data were collected at a speed of 1 °/min, covering a 2θ range of 25°–60°. Pole figures to analyze crystalline texture were obtained from the $[011]_{M1}$ pole in VO_2 using a Bruker D8 x-ray diffraction system (Cu Kα wavelength, 2D detector) with a centric Eulerian cradle at a frame width of 5° for 45 s per frame. The texture results were analyzed with the GADDS software to compile pole figures and then plotted as orientation distribution functions (ODFs) with the MTEX toolbox.[32] Surface analysis of the samples was performed using the Nanosurf FlexAFM system using non-contact mode silicon <10 nm probes with an Al coated reflex side.

Raman maps were collected using a Renishaw inVia microscope using 532 nm excitation with power at the sample of ~50 μW (1% power) and 1 μm sample, with 12 s acquisition time at each pixel. Quantitative phase analysis was performed using the Renishaw wire software non-negative least squares package with respect to non-normalized base spectra considered to be 100% pure (impurities below detection limit) V_2O_5 and VO_2 phases. The pure phase spectrum for V_2O_5 was obtained on a 100 nm calibration sample (same thickness as VO_2 films) averaged over a $10 \times 10\,\mu m^2$ map; no VO_2 Raman peaks were observed anywhere in the map. A pure phase spectrum for VO_2 was obtained on the 100 nm control films over a $10 \times 10\,\mu m^2$ map, but excluding all pixels with any level of detectable V_2O_5 Raman peaks, with only pixels having V_2O_5 peaks below the detection limit contributing to the averaged pure phase VO_2 spectrum. For the control polycrystalline film of VO_2 on SiO_2/Si, small clusters of V_7O_{16} were also detected and excluded from the averaged VO_2 pure phase spectrum. Since pure spectra were non-normalized but taken on the same film thickness, the non-negative least squares regression in each pixel resulted in a value between 0 and 1 directly interpretable as a quantitative phase fraction (see the supplementary material for additional details).

TEM data were obtained on the control and irradiated samples after the final irradiation step. Cross-sectional liftouts of the VO_2 films were prepared for transmission electron microscopy (TEM) analysis using a Thermo Fischer (FEI) Helios gallium focused ion beam (FIB) operating at an accelerating voltage of 30 kV. Protective C, Au, and Pd sputter coating was performed on the samples before exposing them to damaging FIB. Bright-field TEM micrographs (BFTEMs) were acquired using a Thermo Fisher (FEI) Tecnai operating at an accelerating voltage of 200 kV (see Figs. SI-6 and SI-7 in the supplementary material).

C. Device fabrication

Planar four-terminal device structures were fabricated by depositing a 20 nm Ti adhesion layer, followed by 100 nm Au electrode layers on top of the VO_2 thin film using electron beam evaporation. Electrode sizes were defined through maskless lithography (Heidelberg MLA150). Devices were first realigned and then etched using ion milling to create a VO_2 channel with a width of 15–25 μm and a total length of 530 μm. The inner electrode distance was separated by gaps in the range of 40–60 μm [Fig. 3(a)].

D. He irradiation

VO_2 thin films were subjected to 10 keV He^+ ion irradiation using the 10 kV Colutron accelerator at the Sandia Ion Beam Laboratory in Albuquerque, NM. The acceleration energy was 10 keV, and the samples were subjected to irradiation fluences of 5×10^{13}, 1.5×10^{14}, and 5×10^{14} cm^{-2}, where the actual fluence

03 March 2025 14:48:33

© Author(s) 2024

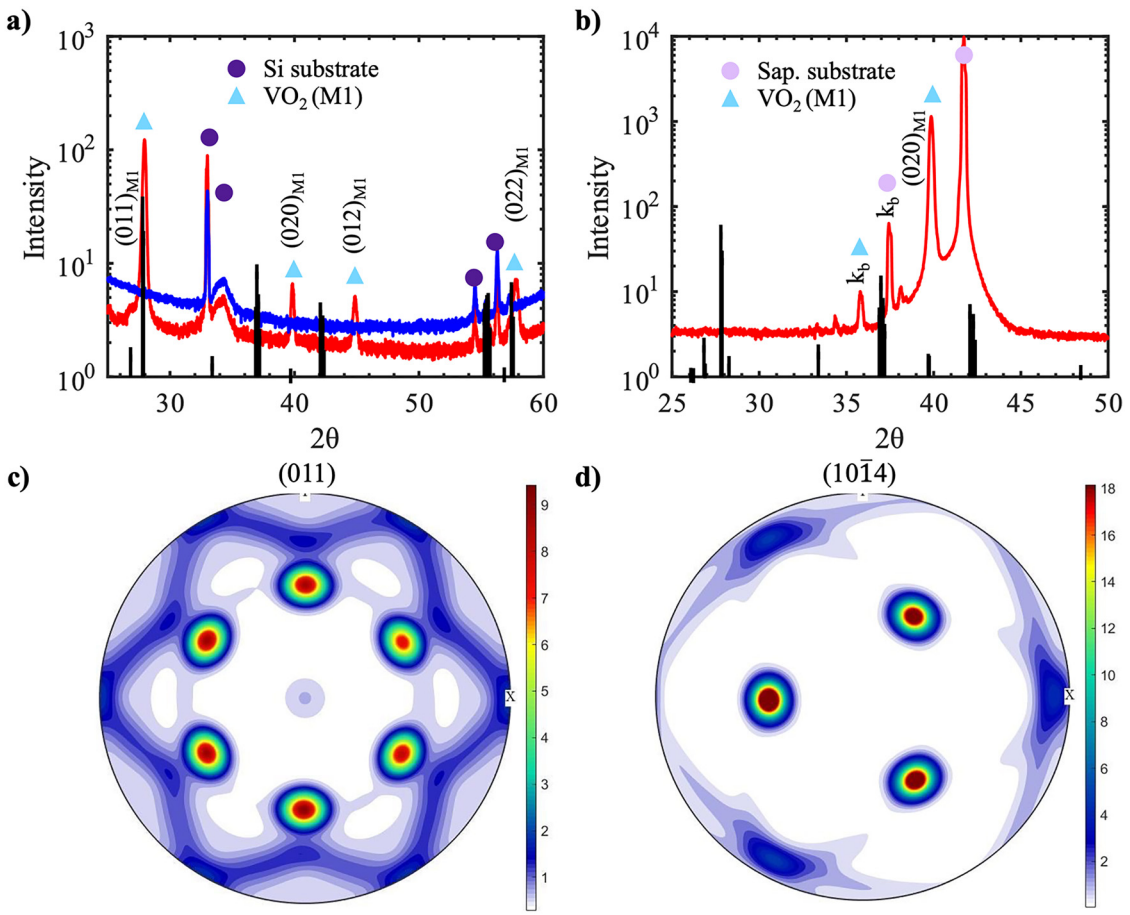

FIG. 2. XRD out of plane scan for (a) as-deposited VO_2 (red) on SiO_2/Si (blue) and (b) VO_2 on Al_2O_3. Additional peaks are present due to spectral contamination from Cu Kβ radiation. The CIF file used for VO_2 M1 is from ICSD #34033, indicated by the black lines in (a) and (b). Pole figures for (c) the VO_2 (011) M1 plane and (d) Al_2O_3 (10$\bar{1}$4) plane. GADDS offline was first used to integrate all frames along a specific 2θ and chi (χ) and plotted as intensity vs 2θ. Here, chi refers to the azimuthal angle of the Debye rings on the 2D detector. The following files (pole figures) were then plotted as (c) and (d) orientation distribution functions (ODFs) using the MTEX toolbox.

values during irradiation are listed in Table II. Low fluences were purposefully picked to modulate electronic transport without disrupting the MIT. The four-terminal devices were fully irradiated with a total film area of 0.3 cm^2 being fully irradiated. The He acceleration energy was selected based on simulations using the Stopping and Range of Ions in Matter (SRIM) software,[33] which predicted a high He^+ concentration implanted residing halfway through the VO_2 layer [Figs. SI-1(a) and SI-1(b) in the supplementary material].

E. Electrical characterization

Electrical characterization was performed using two Keithley 2400 Source Measuring Units attached to a probe station with a heating stage. Film resistivity was determined by measuring the total voltage drop across the two inner terminal probes and the applied current on the two outer probes [Fig. 3(a)]. Each resistivity cycle was obtained from 30–102 °C at a heating/cooling rate of 2 °C/min and a sampling rate of (200 samples/min) to balance data acquisition with data precision. Post-He^+ irradiation, both polycrystalline and quasi-epitaxial films exhibit an initial relaxation process, wherein the resistance of the low-temperature phase measured on heating was lower than that value measured on cooling. To counteract this effect, all samples were cycled through the phase transformation (from 30 to 102 °C) 15 times, after which measured transport data were stable with further cycling. The Seebeck coefficients were measured using a system similar to that previously described.[34] A temperature gradient across the device was generated using the two thermoelectric Peltier modules positioned under each side of the devices with ∼100 μm of gap. The thermoelectric voltage induced by the temperature gradient across the electrodes was obtained using a Keithley 2400 SourceMeter. The temperature gradient was obtained from the difference in the temperature, ΔT, at the film near the two contacts using an IR camera (FLIR

03 March 2025 14:48:33

© Author(s) 2024

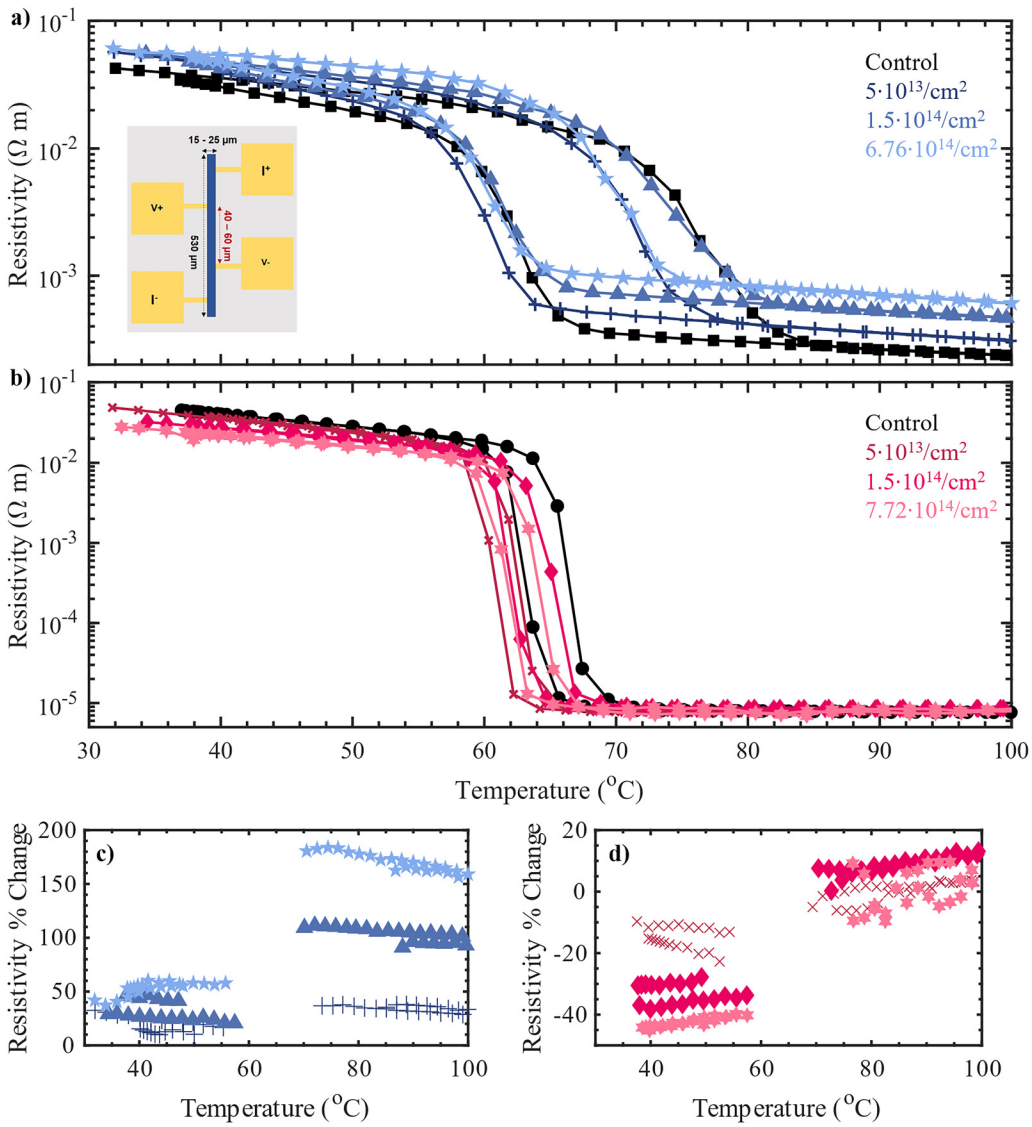

FIG. 3. Electrical four-point measurements of irradiated VO_2 on SiO_2/Si (polycrystalline) and VO_2 on Al_2O_3 (quasi-epitaxial) films. Hysteresis loop of resistivity vs temperature before and after irradiation for samples deposited on (a) SiO_2/Si and (b) Al_2O_3 for different fluences. Measurements for the as-deposited (control) film are plotted in black. Inset in (a) is a schematic of four-terminal devices that were measured to obtain resistivity plots for VO_2 films. Change in the resistivity of the films upon irradiation for VO_2 on (c) SiO_2/Si and (d) Al_2O_3 substrates. In all cases, the same device was irradiated and then measured to eliminate device irregularities.

TABLE II. Irradiation conditions utilized in this study.

Substrate	Energy (keV)	Fluence 1 (ions/cm^{-2})	Fluence 2 (ions cm^{-2})	Fluence 3 (ions/cm^{-2})
SiO_2/Si	10	6.47×10^{13}	1.63×10^{14}	6.78×10^{14}
SiO_2/Si	10	4.99×10^{13}	1.56×10^{14}	6.76×10^{14}
Al_2O_3 (0001)	10	5.06×10^{13}	1.54×10^{14}	7.72×10^{14}
Al_2O_3 (0001)	10	5.06×10^{13}	1.50×10^{14}	5.12×10^{14}

03 March 2025 14:48:33

© Author(s) 2024

SC6700). The Seebeck coefficients of the film were obtained by averaging five different voltage readings at each ΔT and calculating the slope of these points. Seebeck measurements and electrical four-point measurements were completed on the same devices.

The low frequency noise spectra were collected at room temperature under ambient conditions by measuring the current fluctuation from the devices at a 0.5 V bias. The internal biasing circuit of a transimpedance amplifier (Edmund 59–178) applied the voltage bias and amplified the current through the device. The power spectral density of the amplified voltage noise signal (i.e., V^2/Hz) was measured with a Spectrum Analyzer (SR785). Last, the measured voltage noise power spectral density (i.e., V^2/Hz) is converted into current noise power spectral density (i.e., A^2/Hz) using the transimpedance amplifier's gain (e.g., 10^5 A/V).

III. RESULTS

A. Structure of as-deposited VO_2 thin films

The crystal structure of the two different films was characterized by XRD. Figures 2(a) and 2(b) show the XRD spectra of VO_2 thin films before irradiation on SiO_2/Si and single crystal Al_2O_3 substrates, in the 2θ range of 25°–60°. The peaks corresponding to the reflection from the substrate are indicated by circles. The diffraction pattern of the films can be indexed to a monoclinic VO_2 (M1) phase (ICSD #34033). The high-intensity peak at 39.9° indicates that the film on Al_2O_3 is a highly textured system with an orientation along the $(020)_{M1}$ plane. Peaks corresponding to other phases of vanadium oxide, such as V_2O_3 and V_2O_5, have not been observed, suggesting the good phase purity of VO_2 in the films. Peaks at 37° and 42° are not present in the XRD pattern in Fig. 2(a), indicating that some degree of preferred orientation exists in the film. Quasi-epitaxial VO_2 films on $(0001)_{Al2O3}$ contain sixfold in-plane symmetry, supported by the diffraction patterns in Fig. 2(b). Growth for this film occurs in three symmetrically equivalent rotational domains, resulting in a superposition in a diffraction pattern with sixfold symmetry as indicated by the pole figure in Figs. 2(c) and 2(d).[35,36] Texture was obtained by tilting the sample by an angle α at a particular 2θ value. A frame size of 72 frames was picked, which refers to the collection in 5° steps in phi (φ) (i.e., 360°/5° will result in 72 total frames with the sample rotated 5° for each scan).

B. Structural characterization after irradiation

Control and irradiated films were additionally characterized for surface roughness via AFM and quantitative phase composition via Raman mapping. AFM showed a notable impact of substrate on the grain size, with the size of grains deposited on Al_2O_3 being about 1.6 times greater than the ones deposited on the SiO_2/Si substrate (Fig. SI-2 in the supplementary material). Quantitative Raman showed a slight homogenization effect in both sets of films due to irradiation, with the overall mean VO_2 purity being higher in the control, but with substantially V_2O_5 rich inclusions ($0 \leq \phi V_2O_5 \leq 0.4$), whereas after irradiation, the samples had a lower overall VO_2 purity, but the inclusions were less V_2O_5 rich ($0 \leq \phi\ V_2O_5 \leq 0.2$). Here, ϕ refers to the area fraction of a certain phase. Hence, irradiation did not substantially change the phase composition nor seem to cause the growth of a secondary phase. The presence of V_2O_5 as seen in the control is still present after irradiation but with a difference in the spatial distribution (see Figs. SI-3, SI-4, and SI-5 in the supplementary material for additional details).

The microstructure of the VO_2 films is revealed by performing TEM on cross-sectional liftouts of the VO_2 film. We performed overfocusing and underfocusing when imaging the samples. Overall, no major microstructural changes are observed in the microstructure of the film before and after He implantation. Consequently, we infer that the implanted He in the VO_2 films exists at the atomic scale, occupying the interstitial sites as individual He atoms or He atom clusters that are beyond the resolution limit of TEM. The observed differences in transformation behavior and electrical resistance between the as-deposited and He-implanted samples can be attributed to the atomic-level defects created by He implantation. (see Figs. SI-6 and SI-7 in the supplementary material for images and further explanation).

C. Effect of irradiation on electrical transport

1. Temperature-dependent resistivity

Electrical measurements were conducted on the same device before irradiation and after irradiation to different cumulative irradiation exposures, eliminating the device-to-device variation in transport behavior. Electrical measurements were taken within a day after irradiation to prevent potential aging and/or oxidation effects from influencing the results. After the final irradiation, the I–V fits remained linear ensuring good contact between the pads and the VO_2 film. Temperature-dependent resistivity, ρ(T), of as-deposited and He^+ irradiated VO_2 devices on SiO_2/Si and Al_2O_3 substrates, each with distinct ion fluences, was measured by using the standard four-point probe method (Fig. 3). At a temperature of approximately 76.4 and 67 °C, obtained by $\frac{d\log\rho}{dT}$, the as-deposited VO_2 polycrystalline and quasi-epitaxial films exhibited a sharp phase transition from an insulating state to a metallic state, accompanied by a 3 and nearly 4 orders of magnitude change in resistivity, respectively. Following 10 keV He^+ irradiation, the MIT temperature of VO_2 films shifted toward lower values by 3.3 ± 0.025 °C and 1.8 ± 0.024 °C after the final irradiation for polycrystalline and quasi-epitaxial films, respectively. These values were determined by obtaining the maximum of $\frac{d\log\rho}{dT}$ of the heating curves for the films irradiated at the highest fluence. Heating curves were analyzed to be conservative with any reported changes to the MIT. It should be noted that the precision of the calculation of the MIT is at best 2 °C as that is the spacing between data points. The heating/cooling rate of 2 °C/min was determined to be sufficient as this rate is much smaller than the transformation and hysteresis widths for the polycrystalline (18.57 and 14.2 °C) and quasi-epitaxial films (5.79 and 4.0 °C) irradiated at the highest fluence.

The defect populations generated by low-energy irradiation of VO_2 films result in dramatically different changes in charge transport in the two cases (Fig. 3). Interestingly, the impact of irradiation on VO_2 films deposited on SiO_2/Si and Al_2O_3 substrates manifested significantly different resistivities in the low and high-temperature phases. Irradiated devices deposited on the SiO_2/Si

03 March 2025 14:48:33

© Author(s) 2024

substrate demonstrated an increase in resistivity with rising fluence for both phases. The change in resistivity, relative to the as-deposited film, reaches up to 50% and 200% for the low and high-temperature phases, respectively, as illustrated in Fig. 3(c). In contrast, the resistivity of irradiated devices deposited on the Al_2O_3 substrate decreased with increasing fluence during the low-temperature phase (with a resistivity change of up to 50%), while no significant change was observed during the high-temperature phase [see Fig. 3(d)], in agreement with previous studies.[9,18] In summary, electrical resistivity measurements illustrate two critical observations: (1) He^+ irradiation-induced defects impact the electrical transport in insulating monoclinic and metallic rutile phases differently, regardless of the underlying substrate, and (2) the changes in electrical resistivity caused by irradiation were different in films grown on SiO_2/Si in comparison with films grown on Al_2O_3, suggesting that different populations of defects existed in the two cases.

2. Low frequency noise measurements

Low frequency noise measurements have been performed on materials exhibiting a metal–insulator transition such as $La_{0.7}Sr_{0.3}MnO_3$,[37,38] TaO_x,[39] V_2O_3,[40] and VO_2.[41] The noise measurements have been tied to many different mechanisms relating to the size of grains,[42] oxygen vacancies,[37] and percolation of domains across the transition.[39,40] In the case of metallic oxides, low-frequency noise characteristics have been related to the movement of oxygen and strain presence.[43] Thus, noise measurements provide additional insight into the behavior of charge carriers in a semiconducting material.

Flicker noise has a power density spectrum $S(f)$ with a $1/f^{\beta}$ dependency, where f is the frequency and $\beta \approx 1$. Noise arising from resistance fluctuations can be normalized by dividing the current noise by the current flow through the device squared. The empirical relationship in such a normalized power density spectrum proposed by Hooge is often used to compare different systems: $(S_I/I^2)Vf = \alpha/n$, where V is the volume of the sample, n is the carrier density, and α is the dimensionless Hooge parameter.[40,44] As the resistance varied between films, the normalized current noise was considered [Figs. 4(b) and 4(d)] compared to the as collected data in Figs. 4(a) and 4(c). The β exponent of the $1/f^{\beta}$ noise as well as the power density values at 10 Hz for the different devices are summarized in Table III.

Surprisingly, the quasi-epitaxial irradiated VO_2 film exhibited lower noise levels than the control. In the case of polycrystalline VO_2 films, the noise of both the irradiated and the control samples is comparable. The differences in the noise between the two systems indicate that irradiation affects them differently. An irradiated sample exhibiting a lower noise than a control sample may be attributed to the creation of deep trap states. These states then trap defects with energies closer to the conduction band, thereby potentially contributing less to the amplitude of the low frequency noise. These trap states then do not fluctuate and add to the noise created with current flow. It is also possible that irradiation causes the healing of the shallow defects present in the system, where energy transferred from irradiation enables these shallow traps to annihilate. In the case where the level of noise is comparable between as-deposited and irradiated polycrystalline VO_2 films, it is likely that the preexisting defects greatly outnumber the radiation induced defects.

Table III has several entries that are duplicates in the geometry (7 & 8) and in irradiation conditions but with slightly different device dimensions (1 & 2, 3 & 4, 5 & 6). Differences between values in the normalized data can be attributed to device-to-device variability. These differences exist even before irradiation as seen in the normalized power spectrum of the control samples in Figs. 4(b) and 4(d). Furthermore, these measurements were not obtained before and after irradiation like the $\rho(T)$. Each entry corresponds to a different device that was either unirradiated or irradiated.

3. Seebeck measurements

Seebeck measurements were obtained to elucidate the role of carriers in the changes in charge transport. Seebeck data were obtained on control samples and irradiated devices after the last round of irradiation (fluence 3); these same films had been previously imaged via Raman mapping. Several irradiated devices were measured on the same film for repeatability (Fig. 5). Seebeck coefficients were calculated using a linear fit to the data with uncertainty provided. Table IV summarizes the Seebeck coefficients.

Typically, VO_2 has a majority carrier of electrons for both the low- and high-temperature phases.[45] For VO_2 on SiO_2/Si films, the sign of the Seebeck coefficient changes between the control and the irradiated runs. From this observation, we infer that the majority of carriers in the irradiated films are holes rather than electrons. Surprisingly, this trend is not observed in the quasi-epitaxial films, which maintain a negative Seebeck coefficient with little to no change after irradiation. Thus, the observation of the Seebeck coefficients suggests both (1) that irradiation-induced defects affect the number and type of carriers present in the films and (2) that defect populations affect carrier number and types differently in films grown on SiO_2/Si vs films grown on Al_2O_3.

IV. DISCUSSION

A. Effect of He irradiation on the transport properties of VO_2

Changes in overall electrical resistivity in the low-temperature phase and the high-temperature phase ($\rho_{insulating}$ and $\rho_{metallic}$) can generally be attributed to (1) the formation of secondary phases and change in the phase composition of the films, (2) the creation of microscopic defects (cracks, voids, bubbles), (3) the creation of atomic scale defects (vacancies and defect clusters), or some combination thereof. Both Raman mapping and TEM analysis indicate that there is no substantial occurrence of secondary phases resulting from irradiation, suggesting that the first rationale is unlikely. The formation of microscopic defects would tend to uniformly increase the resistivity and would likely have similar effects in both low- and high-temperature phases, which generally were not observed (Fig. 3). On the other hand, observed changes in both Seebeck coefficients, as well as measured noise spectra suggest that either the atomic scale defect populations are different for films grown on different substrates or those resulting defect populations impacted electronic transport differently in the two cases.

03 March 2025 14:48:33

© Author(s) 2024

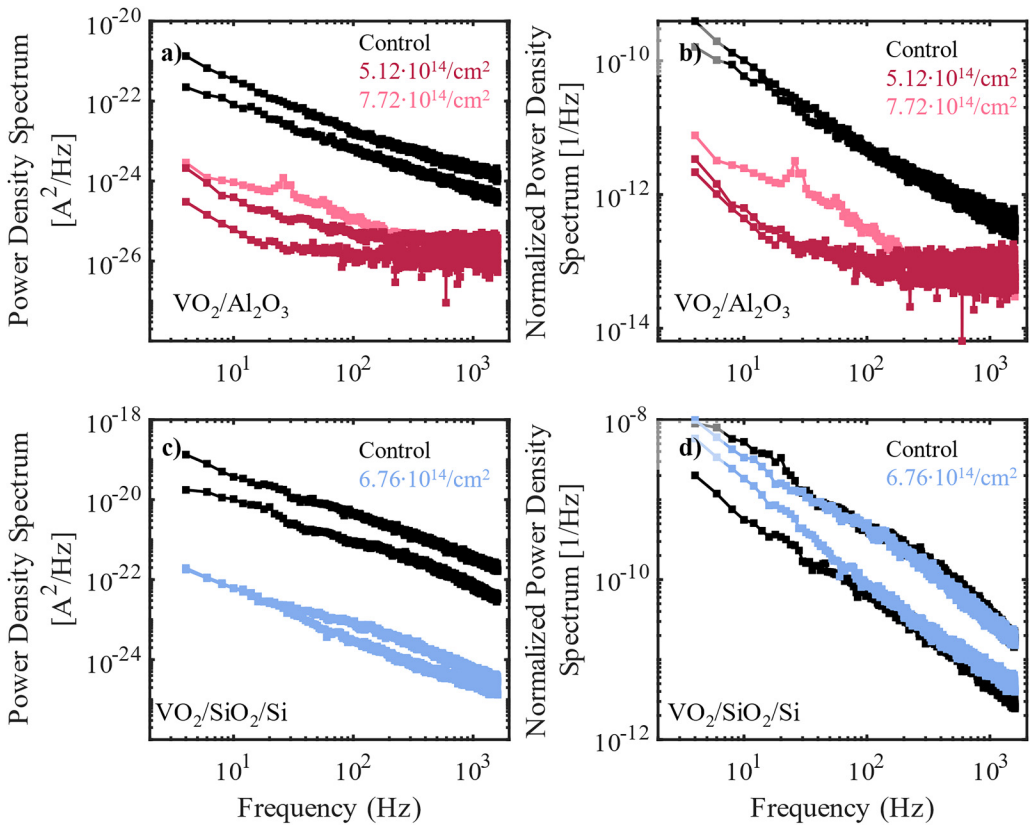

FIG. 4. Low frequency noise measurements resulting in (a) and (c) current noise power density spectrum, $S_I(f)$, and (b) and (d) normalized current noise power density spectrum, $\bar{S}(f) = S_I/I^2$, of (a) and (b) irradiated quasi-epitaxial VO_2 on Al_2O_3 and (c) and (d) irradiated polycrystalline VO_2 on SiO_2/Si films with different fluences. Values for unirradiated control samples are plotted in black, whereas blue and red data points correspond to different irradiation fluences (as in Fig. 3). Multiple repeats are measured, as listed in Table III, indicated by the same color data points.

03 March 2025 14:48:33

Intrinsic point defects in VO_2 films, such as oxygen and vanadium vacancies, interstitials, and anti-site defects, arise naturally during the film deposition process due to kinetic and thermodynamic factors, and they play a crucial role in determining the material's electronic properties. The concentration and distribution of intrinsic defects are highly sensitive to growth conditions such as the synthesis temperature and oxygen partial pressure. Density functional theory (DFT) calculations have been performed to assess

TABLE III. Low frequency noise exponent β and power density values at 10UNDEFINED REF – Hz for different devices.

Device size (L –W) (μm)	Substrate	Fluence (ions/cm^2)	β	Power density at 10 Hz (A^2/Hz)	Normalized Power density at 10 Hz (1/Hz)
60–25	SiO_2/Si	0	1.09	3.71×10^{-20}	5.59×10^{-10}
60–15	SiO_2/Si	0	1.15	1.03×10^{-20}	5.28×10^{-9}
60–25	SiO_2/Si	6.76×10^{14}	1.09	6.03×10^{-23}	3.35×10^{-9}
60–15	SiO_2/Si	6.76×10^{14}	1.12	6.03×10^{-23}	1.83×10^{-9}
60–25	Al_2O_3(0001)	0	1.08	3.48×10^{-22}	5.88×10^{-11}
40–15	Al_2O_3(0001)	0	1.17	8.19×10^{-23}	1.02×10^{-10}
60–25	Al_2O_3(0001)	5.12×10^{14}	0.94	3.93×10^{-25}	4.39×10^{-13}
60–25	Al_2O_3(0001)	5.12×10^{14}	1.15	6.18×10^{-26}	6.29×10^{-13}
60–15	Al_2O_3(0001)	7.72×10^{14}	1.23	9.34×10^{-25}	2.47×10^{-12}

© Author(s) 2024

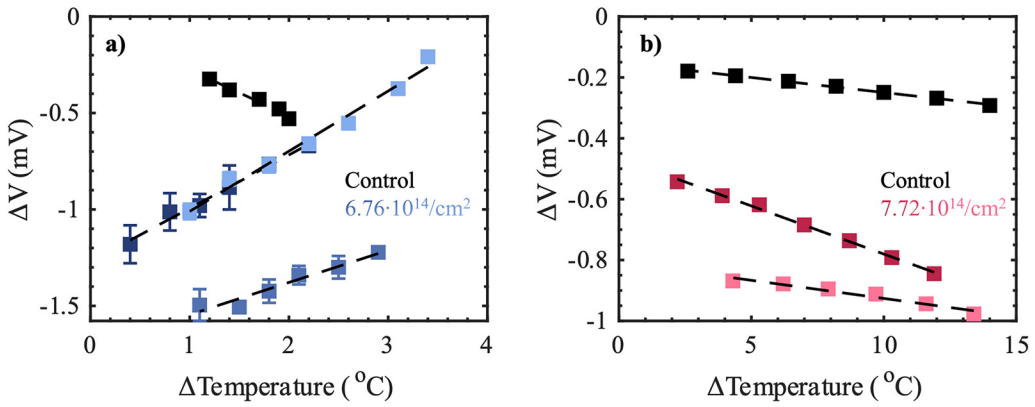

FIG. 5. Seebeck measurements of irradiated VO_2 on (a) SiO_2/Si and (b) Al_2O_3 films. Values for the control sample are plotted in black. A gradient of colors is used to represent the repeat runs on the same sample. Error bars indicate the standard deviation of observations at each temperature difference.

the formation energies of intrinsic point defects in oxygen poor and rich conditions.[46] For instance, it has been shown that oxygen vacancies and vanadium interstitials are the most dominant intrinsic defects in oxygen-rich environments.[47] The population of these defects during the synthesis of the films is very likely, but after irradiation and cycling, the system might not have a chance to thermally equilibrate. While transient defects may be eliminated, there can exist defects that have not reached equilibrium. This system is likely to be different from that considered in the DFT calculations, resulting in the formation of different defects than those theoretically predicted.

The decrease in the electrical resistivity of the low-temperature phase of VO_2 films on Al_2O_3 (0001) substrates with fluence, as seen in Fig. 3(b), is consistent with the creation of additional oxygen vacancies upon irradiation. Due to charge neutrality, the creation of oxygen vacancies can be described as an excess of V with two trapped electrons. In Kroger–Vink notation, this is represented as $O_O^x \Leftrightarrow V_O^{\bullet\bullet} + 2e' + \left(\frac{1}{2}\right)O_2$. Those trapped electrons at the V^{4+} octahedral sites create $V^{(4-n)+}$–V^{4+} pairs with (n = 1, 2, or 3), generating donor levels between the conduction and valence bands.[48,49] With the increase in oxygen vacancies by an increase in the fluence, these donor states also increase. This phenomenon leads to a higher carrier concentration and a shift in the Fermi level of VO_2 toward the conduction band, resulting in reduced resistance within the low-temperature phase.[50–52] Moreover, Seebeck measurements [Fig. 5(b)] indicate that the majority carrier is not changed after irradiation (i.e., electrons), possibly resulting from the extra electrons introduced into the system due to oxygen vacancies. However, Seebeck does show an increase in the coefficient and a decrease in resistivity [Fig. 3(b)], which is unusual, but it is possible that the relaxation time of carriers is being changed with irradiation and is the culprit for this effect. The electrical transport results for the VO_2 on Al_2O_3 have been reported in previous irradiation studies[9,18] and are in good agreement with our data.

In the polycrystalline VO_2 on SiO_2/Si samples, defect generation is evident in the Seebeck data with the majority of carriers changing from electrons to holes after irradiation [Fig. 5(a)]. VO_2 is known to have a majority carrier of electrons[45] regardless of the MIT. Change in the majority carrier species has also been observed in nanowires[53] and in films grown at high temperatures where p-type conductivity has been attributed to the excess of vanadium vacancies.[48] The creation of vanadium vacancies ($V_V^{4\prime}$) can be described as an excess of O with four holes. In Kroger–Vink notation: $O_2 \Leftrightarrow V_V^{4\prime} + 4h^{\bullet} + 2O_O^x$. Trapped holes at the V^{4+} octahedral sites create V^{5+}–V^{4+} pairs with acceptor levels formed above the $d_{||}$ orbital.[48] Given the p-type conduction, as revealed by a positive Seebeck coefficient, two different explanations can account for the increase in resistivity in Fig. 3(a). (1) p-type conduction can lead to an increase of charge carriers with a decrease in mobility, or (2) with p-type conduction, the introduced holes are annihilated by present electrons, which reduces the number of carriers.

In the first case, it would be expected to see a decrease in resistivity if added holes are counted as new carriers. In Fig. 3(a), the opposite occurs: with increasing fluence, the resistivity increases for both the low- and high-temperature phases. Given the relationship between resistivity, mobility (μ), and carrier concentration (n), $\rho = \frac{1}{ne\mu}$, with increasing carrier concentration, the mobility of charge carriers must decrease at a greater rate to justify the increase in the ρ of the monoclinic phase. The significant reduction in carrier mobility can be explained by the higher scattering probability at the grain boundaries in the polycrystalline film that increases with increasing defect density in the film. In the metallic rutile phase, the drastic increase in resistivity with fluence (reaching 200%) can be attributed to scattering only. Since in metals, the charge carriers are delocalized at a constant density, only changes in mobility can explain the substantial change in $\rho_{metallic}$. A similar result was reported in VO_2 films synthesized by atomic layer deposition and bombarded with H_2. With increasing H_2 flow, $\rho_{metallic}$ increased by 2 orders of magnitude while $\rho_{insulating}$ increased by less than an order. The resistivity changes were explained by scattering due to grain boundaries resulting in a lower carrier mobility and stoichiometric shifts.[54] In the second case, however, the addition of holes as predicted by Seebeck can be annihilated with electrons in the system. Therefore, the decrease in the number of

03 March 2025 14:48:33

© Author(s) 2024

TABLE IV. Seebeck values for the control and irradiated films.

Device resistivity (Ω m)	Substrate	Fluence (ions/cm^2)	Seebeck Coeff. (μV/K)
0.035	SiO_2/Si	0 (control)	−236 ± 21.7
0.052	SiO_2/Si	6.7×10^{14}	276 ± 15.5
0.051	SiO_2/Si	6.7×10^{14}	166.9 ± 20.6
0.053	SiO_2/Si	6.7×10^{14}	311.9 ± 17.9
0.034	Al_2O_3 (0001)	0 (control)	−9.9 ± 0.2
0.011	Al_2O_3 (0001)	7.7×10^{14}	−31.6 ± 0.9
0.012	Al_2O_3 (0001)	7.7×10^{14}	−11.9 ± 1.3

carriers would increase the resistivity of the film. Both cases are affected by the mobility of carriers, which is influenced by a combination of lattice scattering and their effective mass. Comparing the mobility between electrons and holes in VO_2 is challenging because, to the best of our knowledge, the effective mass of holes has not yet been calculated. Hence, only the possibility of scattering and annihilation has been considered.

B. The role of the substrate

Despite being irradiated at the same energy and fluences, the polycrystalline VO_2 films exhibited a different response to irradiation than the quasi-epitaxial films. This phenomenon is due to differences in film microstructures in the two cases that could impact either the irradiation cross sections of the two films or the equilibrium concentrations of defects that are likely to remain in a quasi-stable state (i.e., after a small number of cycles). Fundamentally, the differences between the response of the polycrystalline and quasi-epitaxial films must be related to the differences in microstructures between these two systems. Namely, (1) quasi-epitaxial films grown on Al_2O_3 exhibit a degree of strain due to the lattice mismatch between the film and the substrate, (2) quasi-epitaxial films are strongly oriented, with the $[010]_{M1}$ zone axis perpendicular to the Al_2O_3 substrate, and (3) due to their degree of orientation, only a specific sub-population of grain boundaries are likely to exist, which may impact the equilibrium concentration of point defects that exist in the film. These three potential cases will be discussed in more detail below.

Lattice strain could potentially impact both the defect energies and carrier mobilities as well as the MIT temperature. The growth relationship of VO_2 on c-cut Al_2O_3 has been well established, with three different orientations of VO_2 being energetically equivalent.[35,36] A 4% tensile misfit and a 4.4% compressive misfit have been observed along the [010] and [100] directions, respectively. Strained VO_2 films on Al_2O_3 have been shown to exhibit an MIT temperature of up to 77 °C.[55] As films become thicker, for instance, at least 24 nm, studies have shown that the film becomes fully relaxed.[56,57] In this study, the quasi-epitaxial VO_2 films are 100 nm thick, and in Fig. 3(b), ρ(T) data show that the as-deposited film exhibits an MIT temperature of 67 °C. Therefore, the MIT temperature in thick VO_2 quasi-epitaxial films transforms at the bulk temperature, compared with thinner strained films. At the highest fluence, this temperature shifts down to 65 °C as obtained by the $\frac{d\log\rho}{dT}$. By comparison, for the polycrystalline VO_2 films, the MIT temperature is found to be 76.4 and 73.1 °C for the as-deposited and highest fluence samples, respectively. Therefore, since there is no clear indication of a substantial change in the MIT temperature, it seems unlikely that lattice strain from the substrate plays a significant role in the films examined in this study.

Commonly occurring in single crystal materials, accelerated ions are observed to travel further in open directions of the lattice, also known as channeling. Consequently, incident ions can experience anisotropy in energy loss.[58,59] For instance, channeling has been well documented for the [011] of the FCC and [111] of BCC lattices of copper, allowing for deeper penetrations of ions. For our system, the $[010]_{M1}$ zone axis of VO_2 on Al_2O_3 (0001) is perpendicular to the irradiation beam. As in reason (2) stated above, the crystals are all aligned along a particular zone axis where charged particles are less likely to collide with ions in the crystal lattice. In this sense, the radiation cross section is lower, and less damage would be expected to occur. However, if channeling was occurring in the quasi-epitaxial films, then the transport trends would generally be anticipated to be similar in both polycrystalline and quasi-epitaxial films but, to a less extent, in the channeled film due to the presence of less damage. Given the opposite responses in the Seebeck and charge transport, this does not seem to be the case.

In epitaxial films, the prevalence of one specific subpopulation of grain boundaries in the system can change defect–grain boundaries interaction.[60,61] In VO_2, changes in the microstructure of epitaxial films with irradiation have not been well studied compared to other oxides. In an irradiated TiO_2 system, atomistic modeling has shown that grain boundaries and defects interact differently, and their interaction depends on the distance of the grain boundaries from the primary knock off atoms.[60] At intermediate distances, around 4 nm, the grain boundaries will absorb interstitials over vacancies although this bias is removed at close distance. The use of atomistic modeling at pico- to microsecond time scales in Cu revealed that irradiation-induced interstitials were absorbed into the grain boundaries and later emitted to annihilate vacancies several atomic planes away. This recombination mechanism has a lower energy barrier than typical vacancy diffusion and can lead to recovery in materials.[61] In $MgGa_2O_4$ systems, either electrostatic interactions or recombination mechanisms can explain the radiation tolerance of nanocrystalline $MgGa_2O_4$ when irradiated with Kr^{++}, which does not amorphize. In contrast, polycrystalline $MgGa_2O_4$ undergoes amorphization.[62] In all these papers, grain–boundaries–defect interactions are complex and vary with dose and time.

03 March 2025 14:48:33

© Author(s) 2024

The presence of grain boundaries is particularly important when considering transport in the two different systems studied. In the polycrystalline VO_2 film on SiO_2/Si, the flow of charge under the effect of the applied electric field can be described as a function of grain boundaries and the system's bulk energy gap . In the high-temperature phase, the flow of current is only affected by grain boundaries due to the absence of an energy gap. This can explain the changes in electrical transport in Figs. 3(a) and 3(c) where the high-temperature phase has a 200% increase in electrical resistivity. In the quasi-epitaxial films, there exist even fewer grain boundaries, which agrees with the minor resistivity changes in the low-temperature phase and the almost negligible change in the high-temperature phase.

In summary, the difference in response to similar irradiation conditions between quasi-epitaxial and polycrystalline VO_2 films can be attributed to variances in their microstructures. Apparently, neither lattice strain nor channeling in quasi-epitaxial films are responsible for the transport, as the bulk MIT temperature and contrasting transport trends were observed. The presence of grain boundaries may play a crucial role in explaining the distinct charge transport behavior in these systems.[8] In polycrystalline films, grain boundaries influence current flow, leading to a significant increase in the electrical resistivity in the high-temperature phase. In quasi-epitaxial films, the limited number of grain boundaries results in minor resistivity changes in the insulating phase.

V. CONCLUSIONS

He implantation is a viable method for modulating the electrical transport properties of VO_2 thin films by introducing point defects without chemically altering the film's composition. Implantation with a 10 keV He^+ ion beam at ion fluences of 5×10^{13}, 1.5×10^{14}, and $5–7 \times 10^{14}$ cm^{-2} for tuning the electrical properties of VO_2 thin films on SiO_2/Si and Al_2O_3 (0001) substrates has been demonstrated. The different nature of point defects created by He implantation in quasi-epitaxial VO_2 films on Al_2O_3 and in polycrystalline VO_2 films on SiO_2/Si substrates tunes the charge carrier species and mobility, electrical conductivity, and Seebeck coefficient. After irradiating the quasi-epitaxial VO_2 films with 10 keV He^+, the resistivity of the low-temperature insulating phase decreased by 50%, while that of the high-temperature metallic phase remained nearly unchanged. This observation has been attributed to the increase in the carrier concentration upon the creation of oxygen vacancies, which, in turn, enhances the electrical conductivity of VO_2 thin films in the insulating phase. When polycrystalline VO_2 films were irradiated with the same fluences, opposite and different trends in electrical transport properties were observed. The He-implanted films demonstrated an increase in resistivity with rising fluence for both phases. The change in the resistivity, relative to the as-deposited film, reaches up to 50% and 200% for the low and high-temperature phases, respectively. The creation of vanadium vacancies results in an increase in hole carriers where changes in resistivity for the polycrystalline film are a cumulation of competing terms of the carrier density and mobility.

The impact of He implantation on VO_2 films deposited on SiO_2/Si and Al_2O_3 substrates manifested significantly different transport properties in the low and high-temperature phases. We hypothesize that the presence of grain boundaries is crucial for understanding the distinct charge transport behavior in these two systems.

The results discussed herein demonstrate that the irradiation of different microstructures of VO_2 thin films by low-energy He^+ ions provides a promising way for modulating the electrical transport properties, opening the possibility of designing novel nonlinear transport behaviors for modern device fabrication. Furthermore, the observation that the material response to a particular fluence of high energy particles depends on the structure of the film and its underlying substrate implies that different device structures based on different substrates may respond differently to extreme high energy irradiation conditions. This may provide a pathway toward more tunable neuromorphic systems, as well as more resilient electronic systems for space applications.

SUPPLEMENTARY MATERIAL

See the supplementary material for additional information on SRIM-based simulations, AFM, Raman mapping, and TEM; SRIM-based simulations on dpa and resulting He^+ concentrations (Fig. S1); AFM of control samples and after the first round of irradiation (Fig. S2); Raman mapping base spectrum and mapping for control and irradiated films (Figs. S3, S4, and S5); and TEM of control and irradiated samples (Figs. S6 and S7).

ACKNOWLEDGMENTS

This work was primarily supported as part of the Center for Reconfigurable Electronic Materials Inspired by Nonlinear Neuron Dynamics (reMIND), an Energy Frontier Research Center funded by the US Department of Energy, Office of Science, Basic Energy Sciences. VO_2 film growth and characterization were performed at the Texas A&M Engineering Experiment Station under Award No. DE-SC0023353. R.G. acknowledges a graduate fellowship through the NSF under Grant No. DGE:1746932. Film irradiation and device lithography were performed at the Center for Integrated Nanotechnologies, an Office of Science User Facility operated for the US Department of Energy (DOE), Office of Science. Sandia National Laboratories is a multimission laboratory managed and operated by the National Technology & Engineering Solutions of Sandia, LLC, a wholly owned subsidiary of Honeywell International, Inc., for the US DOE's National Nuclear Security Administration under Contract No. DE-NA-0003525. The views expressed in the article do not necessarily represent the views of the US DOE or the United States Government.

03 March 2025 14:48:33

AUTHOR DECLARATIONS

Conflict of Interest

The authors have no conflicts to disclose

Author Contributions

Rebeca M. Gurrola: Data curation (lead); Formal analysis (lead); Methodology (lead); Writing – original draft (lead); Writing – review & editing (lead). **John M. Cain:** Data curation (supporting); Formal analysis (supporting). **Sangheon Oh:** Data curation (supporting). **Timothy D. Brown:** Data curation (supporting); Formal

© Author(s) 2024

analysis (supporting). **Fatme Jardali:** Formal analysis (equal); Methodology (lead); Writing – original draft (supporting); Writing – review & editing (equal). **Ryan M. Schoell:** Data curation (supporting). **Digvijay R. Yadav:** Data curation (supporting); Formal analysis (supporting). **Jiaqi Dong:** Data curation (supporting). **Christopher M. Smyth:** Data curation (supporting). **Matt Pharr:** Resources (supporting). **Suhas Kumar:** Validation (supporting). **Kelvin Xie:** Resources (supporting). **Khalid Hattar:** Resources (supporting); Validation (supporting). **A. Alec Talin:** Formal analysis (supporting); Resources (supporting); Validation (supporting). **Tzu-Ming Lu:** Formal analysis (supporting); Funding acquisition (supporting); Resources (supporting); Validation (supporting). **Patrick J. Shamberger:** Conceptualization (equal); Formal analysis (equal); Funding acquisition (equal); Resources (equal); Supervision (equal); Validation (equal); Writing – original draft (equal); Writing – review & editing (equal).

DATA AVAILABILITY

The data that support the findings of this study are available from the corresponding author upon request.

REFERENCES

[1]F. J. Morin, Phys. Rev. Lett. **3**, 34 (1959).
[2]J. B. Goodenough, J. Solid State Chem. **3**, 490 (1971).
[3]P. Schofield, A. Bradicich, R. M. Gurrola, Y. Zhang, T. D. Brown, M. Pharr, P. J. Shamberger, and S. Banerjee, Adv. Mater. **35**, 2205294 (2023).
[4]W. Yi, K. K. Tsang, S. K. Lam, X. Bai, J. A. Crowell, and E. A. Flores, Nat. Commun. **9**, 4661 (2018).
[5]E. Kusano and J. A. Theil, J. Vac. Sci. Technol. A **7**, 1314 (1989).
[6]Z. Zhang, F. Zuo, C. Wan, A. Dutta, J. Kim, J. Rensberg, R. Nawrodt, H. H. Park, T. J. Larrabee, X. Guan, Y. Zhou, S. M. Prokes, C. Ronning, V. M. Shalaev, A. Boltasseva, M. A. Kats, and S. Ramanathan, Phys. Rev. Appl. **7**, 034008 (2017).
[7]H. Yoon, M. Choi, T. W. Lim, H. Kwon, K. Ihm, J. K. Kim, S. Y. Choi, and J. Son, Nat. Mater. **15**, 1113 (2016).
[8]D. Brassard, S. Fourmaux, M. Jean-Jacques, J. C. Kieffer, and M. A. El Khakani, Appl. Phys. Lett. **87**, 051910 (2005).
[9]G. R. Khan, A. Kandasami, and B. A. Bhat, Radiat. Phys. Chem. **123**, 55 (2016).
[10]K. Nagashima, T. Yanagida, H. Tanaka, and T. Kawai, Phys. Rev. B **74**, 172106 (2006).
[11]Y. Muraoka, K. Saeki, R. Eguchi, T. Wakita, M. Hirai, T. Yokoya, and S. Shin, J. Appl. Phys. **109**, 043702 (2011).
[12]S. Fan, L. Fan, Q. Li, J. Liu, and B. Ye, Appl. Surf. Sci. **321**, 464 (2014).
[13]S. Kittiwatanakul, J. Laverock, D. Newby, K. E. Smith, S. A. Wolf, and J. Lu, J. Appl. Phys. **114**, 053703 (2013).
[14]Y. Cui and S. Ramanathan, J. Vac. Sci. Technol. A **29**, 041502 (2011).
[15]J. Ziegler, *Handbook of Ion Implantation Technology* (Press Inc., 1992).
[16]J. M. P. J. S. Williams, *Ion Implantation and Beam Processing* (Academic Press, 2014).
[17]B. M. Mabakachaba, Master of Science Thesis, (University of the Western Cape, 2020).
[18]J. G. Ramirez, T. Saerbeck, S. Wang, J. Trastoy, M. Malnou, J. Lesueur, J.-P. Crocombette, J. E. Villegas, and I. K. Schuller, Phys. Rev. B **91**, 205123 (2015).
[19]E. M. Heckman, L. P. Gonzalez, S. Guha, J. O. Barnes, and A. Carpenter, Thin Solid Films **518**, 265 (2009).
[20]L. A. Gea and L. A. Boatner, Appl. Phys. Lett. **68**, 3081 (1996).
[21]J. Rensberg, S. Zhang, Y. Zhou, A. S. Mcleod, C. Schwarz, M. Goldflam, M. Liu, J. Kerbusch, R. Nawrodt, S. Ramanathan, D. N. Basov, F. Capasso, C. Ronning, and M. A. Kats, Nano Lett. **16**, 1050 (2016).
[22]K. D. Ufert, Phys. Status Solidi A **42**, 187 (1977).
[23]P. Jin, S. Nakao, and S. Tanemura, Nucl. Instrum. Methods Phys. Res., Sect. B **141**, 419 (1998).
[24]P. Jin, S. Nakao, and S. Tanemura, Thin Solid Films **324**, 151 (1998).
[25]B. M. Mabakachaba, I. G. Madiba, J. Kennedy, K. Kaviyarasu, P. Ngoupe, B. S. Khanyile, J. J. Van Rensburg, F. Ezema, C. J. Arendse, and M. Maaza, Surf. Interfaces **20**, 100590 (2020).
[26]H. Lim, N. Stavrias, B. C. Johnson, R. E. Marvel, R. F. Haglund, and J. C. Mccallum, J. Appl. Phys. **115**, 093107 (2014).
[27]A. Gupta, R. Singhal, J. Narayan, and D. K. Avasthi, J. Mater. Res. **26**, 2901 (2011).
[28]L. Jin, Y. Shi, F. I. Allen, L.-Q. Chen, and J. Wu, Phys. Rev. Lett. **129**, 245701 (2022).
[29]W. Fan, J. Cao, J. Seidel, Y. Gu, J. W. Yim, C. Barrett, K. M. Yu, J. Ji, R. Ramesh, L. Q. Chen, and J. Wu, Phys. Rev. B **83**, 235102 (2011).
[30]A. Leone, A. M. Trione, and F. Junga, IEEE Trans. Nucl. Sci. **37**, 1739 (1990).
[31]H. Karl and S. C. Peyinghaus, Nucl. Instrum. Methods Phys. Res., Sect. B **365**, 75 (2015).
[32]F. Bachmann, R. Hielscher, and H. Schaeben, Solid State Phenomena **160**, 63 (2010).
[33]J. F. Ziegler, M. D. Ziegler, and J. P. Biersack, Nucl. Instrum. Methods Phys. Res., Sect. B **268**, 1818 (2010).
[34]K. J. Erickson, F. Leonard, V. Stavila, M. E. Foster, C. D. Spataru, R. E. Jones, B. M. Foley, P. E. Hopkins, M. D. Allendorf, and A. A. Talin, Adv. Mater. **27**, 3453 (2015).
[35]T.-H. Yang, R. Aggarwal, A. Gupta, H. Zhou, R. J. Narayan, and J. Narayan, J. Appl. Phys. **107**, 053514 (2010).
[36]L. L. Fan, Y. F. Wu, C. Si, G. Q. Pan, C. W. Zou, and Z. Y. Wu, Appl. Phys. Lett. **102**, 011604 (2013).
[37]P. Orgiani, A. Y. Petrov, R. Ciancio, A. Galdi, L. Maritato, and B. A. Davidson, Appl. Phys. Lett. **100**, 042404 (2012).
[38]L. Méchin, S. Wu, B. Guillet, P. Perna, C. Fur, S. Lebargy, C. Adamo, D. G. Schlom, and J. M. Routoure, J. Phys. D: Appl. Phys. **46**, 202001 (2013).
[39]W. Yi, S. E. Savel'ev, G. Medeiros-Ribeiro, F. Miao, M. X. Zhang, J. J. Yang, A. M. Bratkovsky, and R. S. Williams, Nat. Commun. **7**, 11142 (2016).
[40]L. Chen, P. Zhou, Y. Kalcheim, I. K. Schuller, and D. Natelson, APL Mater. **8**, 101103 (2020).
[41]Z. Topalian, S.-Y. Li, G. A. Niklasson, C. G. Granqvist, and L. B. Kish, J. Appl. Phys. **117**, 025303 (2015).
[42]X. Liu, Z. Jiao, K. Nakamura, T. Hatano, and Y. Zeng, J. Appl. Phys. **87**, 2431 (2000).
[43]A. K. Raychaudhuri, Curr. Opin. Solid State Mater. Sci. **6**, 67 (2002).
[44]S. Kogan, *Electronic Noise and Fluctuations in Solids* (Cambridge University Press, Cambridge, 2008).
[45]C. N. Berglund and H. J. Guggenheim, Phys. Rev. **185**, 1022 (1969).
[46]Y. Cui, B. Liu, L. Chen, H. Luo, and Y. Gao, AIP Adv. **6**, 105301 (2016).
[47]D. G. Sellers, E. J. Braham, R. Villarreal, B. Zhang, A. Parija, T. D. Brown, T. E. G. Alivio, H. Clarke, L. R. De Jesus, L. Zuin, D. Prendergast, X. Qian, R. Arroyave, P. J. Shamberger, and S. Banerjee, J. Am. Chem. Soc. **142**, 15513 (2020).
[48]C. Chen, Y. Zhao, X. Pan, V. Kuryatkov, A. Bernussi, M. Holtz, and Z. Fan, J. Appl. Phys. **110**, 023707 (2011).
[49]G. Liu, F. Li, D. W. Wang, D. M. Tang, C. Liu, X. Ma, G. Q. Lu, and H. M. Cheng, Nanotechnology **19**, 025606 (2008).
[50]L. L. Fan, S. Chen, G. M. Liao, Y. L. Chen, H. Ren, and C. W. Zou, J. Phys.: Condens. Matter. **28**, 255002 (2016).
[51]S. A. Ansari, M. M. Khan, S. Kalathil, A. Nisar, J. Lee, and M. H. Cho, Nanoscale **5**, 9238 (2013).
[52]S. Chen, X. j. Wang, L. Fan, G. Liao, Y. Chen, W. Chu, L. Song, J. Jiang, and C. Zou, Adv. Funct. Mater. **26**, 3532 (2016).
[53]X. Peng, Y. Yang, Y. Hou, H. C. Travaglini, L. Hellwig, S. Hihath, K. van Benthem, K. Lee, W. Liu, and D. Yu, Phys. Rev. Appl. **5**, 054008 (2016).

03 March 2025 14:48:33

© Author(s) 2024

[54]H. H. Park, T. J. Larrabee, L. B. Ruppalt, J. C. Culbertson, and S. M. Prokes, ACS Omega **2**, 1259 (2017).
[55]A. Moatti, R. Sachan, J. Prater, and J. Narayan, ACS Appl. Mater. Interfaces **9**, 24298 (2017).
[56]L. L. Fan, S. Chen, Z. L. Luo, Q. H. Liu, Y. F. Wu, L. Song, D. X. Ji, P. Wang, W. S. Chu, C. Gao, C. W. Zou, and Z. Y. Wu, Nano Lett. **14**, 4036 (2014).
[57]C. Chen, Y. Zhu, Y. Zhao, J. H. Lee, H. Wang, A. Bernussi, M. Holtz, and Z. Fan, Appl. Phys. Lett. **97**, 211905 (2010).
[58]M. T. Robinson and O. S. Oen, Phys. Rev. **132**, 2385 (1963).
[59]C. Erginsoy, H. E. Wegner, and W. M. Gibson, Phys. Rev. Lett. **13**, 530 (1964).
[60]X. M. Bai and B. P. Uberuaga, Philos. Mag. **92**, 1469 (2012).
[61]X. M. Bai, A. F. Voter, R. G. Hoagland, M. Nastasi, and B. P. Uberuaga, Science **327**, 1631 (2010).
[62]T. D. Shen, S. Feng, M. Tang, J. A. Valdez, Y. Wang, and K. E. Sickafus, Appl. Phys. Lett. **90**, 263115 (2007).
[63]L. Jin, S. E. Zeltmann, H. S. Choe, H. Liu, F. I. Allen, A. M. Minor, and J. Wu, Phys. Rev. B **102**, 041120 (2020).

03 March 2025 14:48:33

© Author(s) 2024